

¹ **Space-Time Ambiguity Functions for** ² **Electronically Scanned ISR Applications**

John Swoboda,¹ Joshua Semeter,¹ Philip Erickson²

Corresponding author: J. P. Swoboda, Department of Electrical & Computer Engineering,
Boston University, 8 Saint Marys Street Boston, MA 02215, USA. (swoboj@bu.edu)

¹Department of Electrical & Computer
Engineering, Boston University, Boston,
Massachusetts, USA.

²Haystack Observatory, Massachusetts
Institute of Technology, Westford,
Massachusetts, USA.

Electronically steerable array (ESA) technology has recently been applied to incoherent scatter radar (ISR) systems. These arrays allow for pulse-to-pulse steering of the antenna beam to collect data in a three dimensional region. This is in direct contrast to dish based antennas, where ISR acquisition is limited at any one time to observations in a two dimensional slice. This new paradigm allows for more flexibility in the measurement of ionospheric plasma parameters.

Multiple ESA based ISR systems operate currently in the high latitude region where the ionosphere is highly variable in both space and time. Because of the highly dynamic nature of the ionosphere in this region, it is important to differentiate between measurement induced artifacts and the true behavior of the plasma. Often three dimensional ISR data produced by ESA techniques are fitted in a spherical coordinate space and then the parameters are interpolated to a Cartesian grid, introducing potential error and impacting the reconstructions of the plasma parameters.

To take advantage of the new flexibility inherent in ESA systems, we present a new way of analyzing ISR observations through use of the space-time ambiguity function. This concept is similar to the range ambiguity function that is used in traditional ISR for scanning antenna systems, but we have extended the concept to all spatial dimensions along with time as well.

The use of this new measurement ambiguity function allow us to pose the ISR observational problem in terms of a linear inverse problem whose goal

25 is measurement of the time domain lags of the intrinsic plasma autocorre-
26 lation function. The framework allows us to explore the impact of non-uniformity
27 in plasma parameters in both time and space. We discuss examples of pos-
28 sible artifacts in high latitude situations, and explore ways of reducing them
29 and improving the quality of data products from electronically steerable ISRs.

1. Introduction

Incoherent scatter radar (ISR) is a powerful tool for exploring the ionosphere. These systems can give measurements of electron density N_e , ion temperature T_i , electron temperature T_e , ion velocity V_i and other plasma parameters [Dougherty and Farley, 1960; Farley et al., 1961; Dougherty and Farley, 1963; Hagfors, 1961]. These parameters are measured by fitting a nonlinear first-principles, physics based autocorrelation function (ACF) model to an estimated time autocorrelation or, alternatively, the power spectrum of the radar signal scattered off of random electron density fluctuations [Lehtinen and Huuskonen, 1996].

This is an estimation of a second order statistic of an inherently random process from the scattering of electrons. In order to get an estimate of the ACF with reasonable statistical properties, an ensemble average must be performed by averaging pulses together. With traditional dish antennas, ISR systems build statistics in a limited number of ways. One method consists of pointing the radar beam in a specific direction and dwelling until enough pulses are integrated to get the desired statistics. Alternatively, the beam can be scanned through a field of view, collecting pulses while moving. These techniques use an implicit assumption about the uniformity of the plasma parameters within a volume defined by the pulse shape and solid angle beam properties while pulses are being integrated. This leads to an assumption of stationarity of the ACF within a temporal and spatial resolution cell of the radar.

In many cases, especially in the high latitude ionosphere, this stationarity assumption is not met. Phenomena such as polar cap patches can drift at greater than

1 km/s, and thus the residency time of a particular plasma parcel within a radar beam may be much shorter than the integration time required to estimate an ACF [Dahlgren *et al.*, 2012a]. In the auroral zone, ionospheric variations produced by auroral particle precipitation occur on similarly short time scales compared to the integration period [Zettergren *et al.*, 2008].

Recently, electronically steerable array (ESA) technology has started to be leveraged by the ISR community. The Advanced Modular Incoherent Scatter Radar (AMISR) systems have already been deployed both at the Poker Flat Alaska (PFISR) and Resolute Bay Canada (RISR) geospace facilities. The European led EISCAT-3D project is currently being developed using phased array technology as well and will be capable of multistatic processing. These new systems are already being used in a number of different ways including creating volumetric reconstructions of plasma parameters [Semeter *et al.*, 2009; Nicolls and Heinselman, 2007; Dahlgren *et al.*, 2012a, b]. These reconstructions primarily consist of recasting ISR data into a Cartesian space through interpolation, after parameters have first been fit in a spherical coordinate system.

These new ESA based systems differentiate themselves from dish antennas in a fundamental way. Instead of dwelling in a single beam or scanning along a prescribed direction, an ESA can move to a different beam position within its field of view on a rapid, pulse by pulse basis. This yields a new flexibility to statistically combine information from different beams using knowledge of the plasma velocity field, where this information is obtained either from external sources or from the Doppler shift of the

ionospheric echoes themselves. This can help to relax the assumption of stationarity, since if the plasma moves into a different beam, returns from the same plasma can be integrated together with proper bookkeeping. Such a technique is very difficult to accomplish with dish antenna based systems having significant pointing inertia, and typically in these situations the returns from different plasmas are unavoidably and improperly averaged together.

In order to take advantage of new ESA flexibilities, this work puts forth the idea of the space-time ambiguity function. This concept extends the range ambiguity to all three spatial dimensions along with time. The goal of this paper is to develop the formalism for treating space-time ambiguity for electronically steerable ISRs, and in particular ISRs that are capable of sampling a given volume on a pulse-by-pulse basis. We will develop specific cases of the impact of the three-dimensional ambiguity on moving plasma using conditions characteristic of polar cap patches. A simulation of a polar cap patch using a full ISR simulator, which creates ISR data at the I/Q level, will be shown. Lastly we will explore a number of different strategies that could improve measurements from electronically steerable ISR systems.

2. Space-Time Ambiguity

The space-time ambiguity can be thought of as a kernel to a combined volume and time integration operator. This ambiguity can be represented as a kernel operator in a Fredholm integral equation:

$$\rho(\tau_s, \mathbf{r}_s, t_s) = \int L(\tau_s, \mathbf{r}_s, t_s, \tau, \mathbf{r}, t) R(\tau, \mathbf{r}, t) d\mathbf{r} dt d\tau \quad (1)$$

where, for ISR, $R(\tau, \mathbf{r}, t)$ is the lag τ of the autocorrelation function at time t , and position \mathbf{r} .

By using this formulation, many parallels between ISR and classic camera blurring problems can be made. In cameras, blurring can take place when an object moves over a space covered by one pixel while the shutter is open and the CCD is collecting photons. A diagram of this can be seen in Figure 1. The same holds for the ISR measurement problem, except that the pixels are no longer square and instead are determined by the beam shape and pulse pattern. This is shown in the diagrams in Figure 2.

2.1. Coordinate System Definitions

Before we derive the full space-time ambiguity function $K(\mathbf{r}_s, \mathbf{r})$ we will start with defining our coordinate system. Our three dimensional coordinate system is defined as $\mathbf{r} = [x, y, z]^T$. For this coordinate system, $\mathbf{r} = [0, 0, 0]^T$ at the location of the radar and thus $r = |\mathbf{r}|$, also known as the range variable. This allows for the use of polar coordinates $\mathbf{r} = [r, \theta, \phi]^T$ where θ is the observer's elevation angle and ϕ is the azimuth angle.

The radar samples this space at a set of discrete points which will be referred to as $\mathbf{r}_s = [x_s, y_s, z_s]^T$ along with the discretized range expression $r_s = |\mathbf{r}_s|$. The sampled space consists of a number of points, composed of range gates within a beam multiplied by the number of beams. These points can also be referred in polar

111 coordinates $\mathbf{r}_s = [r_s, \theta_s, \phi_s]^T$, where θ_s is the observationally sampled elevation angle
 112 and ϕ_s is the sampled azimuth angle.

113 For notation purposes, we use two different sets of time commonly known in radar
 114 literature as fast-time, n and slow-time, t [Richards, 2005]. Fast-time is used to
 115 describe processes with correlation time less than one pulse repetition interval (PRI).
 116 Slow-time will be used for processes that decorrelate in time on the order of, or longer
 117 than, the system's PRI. In order to form estimates of ACFs with desired statistical
 118 properties, it is assumed that the plasma parameters will change on the
 119 order of many tens to hundreds of PRIs in their stationary reference frame (i.e. remain
 120 wide sense stationary for this time). Generally for incoherent scatter applications in
 121 the E-region of the ionosphere (100 km altitude) and above, the decorrelation time
 122 is less than a PRI, and thus ACFs must be formed over fast-time.

123 The terms n and t represent continuous variables, while n_s and t_s will be the fast
 124 time and slow time parameters sampled by the radar. The sampling rate of n_s is
 125 set by the rate at which the system's A/D converters are run. The sampling of t_s
 126 can, at the highest rate, be the PRI. At its lowest rate, it can be sampled once in a
 127 non-coherent processing interval (NCPI), or equivalently in a period of time it takes
 128 the radar to average the desired number of pulses.

2.2. Derivation

129 The basic physical mechanism behind ISR produces measurable radar scatter from
 130 electron density fluctuations in the ionosphere, $n_e(\mathbf{r}, n)$. These fluctuations scatter
 131 radio waves which can be observed by the receiver system of the radar [Dougherty

132 *and Farley, 1960*]. The emitted radar signal at the transmitter has a pulse shape
 133 $s(n)$ modulated at a central frequency creating a scattering wave number \mathbf{k} . Using
 134 the Born approximation, the signal received at time n , $x(n)$, can be represented as
 135 the following

$$x(n) = h(n) * \int \exp[-j\mathbf{k} \cdot \mathbf{r}] s\left(n - \frac{2r}{c}\right) n_e(\mathbf{r}, n) d\mathbf{r}, \quad (2)$$

136 where $h(n)$ is the receiver filter and the $*$ represents the convolution operator. In
 137 modern ISR systems, this signal $x(n)$ is then sampled at discrete points in fast-time
 138 which will be referred to as n_s . The convolution and sampling operation can be
 139 brought in the integral as the following,

$$x(n_s) = \int \exp[-j\mathbf{k} \cdot \mathbf{r}] s\left(n - \frac{2r}{c}\right) n_e(\mathbf{r}, n) h(n_s - n) d\mathbf{r} dn \quad (3)$$

140 Once the signal has been received and sampled, the autocorrelation function is
 141 then estimated from the sampled signal $x(n_s)$. The full expression of the underlying
 142 autocorrelation of this signal is the following,

$$\begin{aligned} \langle x(n_s) x^*(n'_s) \rangle &= \int \exp[-j\mathbf{k} \cdot (\mathbf{r}' - \mathbf{r})] s\left(n - \frac{2r}{c}\right) s^*\left(n' - \frac{2r'}{c}\right) \\ &\quad h(n_s - n) h(n'_s - n') \langle n_e(\mathbf{r}, n) n_e^*(\mathbf{r}', n') \rangle d\mathbf{r} d\mathbf{r}' dn dn', \quad (4) \end{aligned}$$

143 where r' is the magnitude of the vector \mathbf{r}' . By assuming stationarity of second order
 144 signal statistics along fast time, we can then substitute the lag variables $\tau \equiv n' - n$,
 145 and $\tau_s \equiv n'_s - n_s$. With these substitutions, Equation 4 becomes

$$\langle x(n_s)x^*(n_s + \tau_s) \rangle = \int \exp[-j\mathbf{k} \cdot (\mathbf{r}' - \mathbf{r})] s\left(n - \frac{2r}{c}\right) s^*\left(n + \tau - \frac{2r'}{c}\right) h(n_s - n)h(n_s + \tau_s - n - \tau) \langle n_e(\mathbf{r}, n)n_e^*(\mathbf{r}', n + \tau) \rangle d\mathbf{r}d\mathbf{r}'dn d\tau \quad (5)$$

146 We can make a simplifying assumption at this point that the space-time autocorre-
 147 lation function of $n_e(\mathbf{r}, t)$, $\langle n_e(\mathbf{r}, n)n_e(\mathbf{r}', n + \tau) \rangle$, will go to zero as the magnitude of
 148 $\mathbf{y} \equiv \mathbf{r}' - \mathbf{r}$ increases beyond the debye length [Farley, 1969]. Thus, the rate which
 149 the spatial autocorrelation goes to zero will be such that $\tau \gg \frac{2\|\mathbf{y}\|}{c}$, allowing us to
 150 set $r = r'$. This allows Equation 5 to be rewritten as

$$\langle x(n_s)x^*(n_s + \tau) \rangle = \int s\left(n - \frac{2r}{c}\right) s^*\left(n + \tau - \frac{2r}{c}\right) h(n_s - n)h^*(n_s + \tau_s - n - \tau) \left[\int \exp[-2j\mathbf{k} \cdot \mathbf{y}] \langle n_e(\mathbf{r}, n)n_e^*(\mathbf{y} + \mathbf{r}, n + \tau) \rangle d\mathbf{y} \right] d\mathbf{r}dn d\tau. \quad (6)$$

The inner integral is a spatial Fourier transform evaluated at the wave number of the radar \mathbf{k} . By again asserting stationarity along fast time, we can represent the true ACF as the following,

$$R(\tau, \mathbf{r}) = \langle |n_e(\mathbf{k}, r, \tau)|^2 \rangle \equiv \int \exp[-2j\mathbf{k} \cdot \mathbf{y}] \langle n_e(\mathbf{r}, b)n_e^*(\mathbf{y} + \mathbf{r}, n + \tau) \rangle d\mathbf{y}. \quad (7)$$

151 Now Equation 6 becomes

$$\langle x(n_s)x^*(n_s + \tau_s) \rangle = \int \langle |n_e(\tau, \mathbf{k}, \mathbf{r})|^2 \rangle \left[\int s\left(n - \frac{2r}{c}\right) s^*\left(n + \tau - \frac{2r}{c}\right) h(n_s - n)h^*(n_s + \tau_s - n - \tau) dn \right] d\tau dr. \quad (8)$$

If n_s is replaced with $2r_s/c$ we can introduce the range ambiguity function $W(\tau_s, r_s, \tau, r)$ by doing the following substitution,

$$W(\tau_s, r_s, \tau, r) = \int s(n - \frac{2r}{c}) s^*(n + \tau - \frac{2r}{c}) h(2r_s/c - n) h^*(2r_s/c + \tau_s - n - \tau) dn. \quad (9)$$

Assuming, for the moment, that $R(\tau, \mathbf{r})$ only varies across the range dimension r , we can now represent this in the form of a Fredholm integral equation

$$\langle x(2r_s/c) x^*(2r_s/c + \tau_s) \rangle = \int W(\tau_s, r_s, \tau, r) R(\tau, r) dr d\tau. \quad (10)$$

The range ambiguity function, $W(\tau_s, r_s, \tau, r)$, can be thought of as a smoothing operator along the range and lag dimensions of $R(\tau, r)$.

The spatial ambiguity across azimuth and elevation angles is determined by the antenna beam pattern. In phased array antennas, this beam pattern is ideally the array factor multiplied by the element pattern [Balanis, 2005]. The array factor is determined by a number of things including the element spacing and the wave number of the radar, k . For example, by making idealized assumptions with no mutual coupling and that the array elements are cross dipole elements, AMISR systems will have the following antenna pattern for pointing angle (θ_s, ϕ_s) :

$$F(\theta_s, \phi_s, \theta, \phi) = \frac{1}{2}(1 + \cos(\theta)^2) \left[\frac{1}{MN} (1 + \exp[j(\psi_y/2 + \psi_x)]) \frac{\sin((M/2)\psi_x)}{\sin(\psi_x)} \frac{\sin((N/2)\psi_x)}{\sin(\psi_x/2)} \right]^2, \quad (11)$$

where $\psi_x = -kd_x(\sin \theta \cos \phi - \sin \theta_s \cos \phi_s)$, $\psi_y = -kd_y(\sin \theta \sin \phi - \sin \theta_s \sin \phi_s)$ and M is the number of elements in the x direction of the array, and N is the number of elements in the y direction (see Appendix: A for derivation).

The spatial ambiguity is a separable function made up of the components of $W(\tau_s, \tau, r_s, r)$ and $F(\theta_s, \phi_s, \theta, \phi)$. These two functions can be combined by multiplying the two, creating the spatial ambiguity function $K(\tau_s, \mathbf{r}_s, \tau, \mathbf{r})$, and then doing a volume integration. This yields an expression for a single statistical realization of the ACF of the incoherent scatter random process, which will be referred to as $\rho(\tau_s, \mathbf{r}_s)$:

$$\rho(\tau_s, \mathbf{r}_s) = \int F(\theta_s, \phi_s, \theta, \phi) W(\tau_s, r_s, \tau, r) R(\tau, \mathbf{r}) dV, \quad (12)$$

$$= \int K(\tau_s, \mathbf{r}_s, \tau, \mathbf{r}) R(\tau, \mathbf{r}) dV. \quad (13)$$

A rendering of an example of this full spatial ambiguity function for an uncoded long pulse, with antenna pattern from Equation 11 for four beams, can be seen in Figure 3.

As mentioned above, this one pulse ACF estimate represents a single sample of a random process. In order to create a usable estimate, multiple samples of this ACF need to be averaged together to reduce the variance to sufficient levels in order to fit the estimate to a theoretical ACF that is a direct function of plasma parameter values. To show the impact of this averaging in creating the estimate of the ACF, we will add slow-time dependence to the expression for the medium ACF, which now becomes $R(\tau, \mathbf{r}, t)$, and will also add another separable function $G(t_s, t)$ to the kernel. This function $G(t_s, t)$ can be thought of as a sampling and blurring kernel for the ACF if the plasma parameters change within an NCPI. Since the amount of time that

the radar pulse is illuminating the plasma in a point of space is very short compared to IPP, $G(t_s, t)$ can take the form of a summation of Dirac delta functions

$$G(t_s, t) = \sum_{j=0}^{J-1} \alpha_j \delta(t - t_s - jT_{PRI}), \quad (14)$$

where J is the number of pulses used over a NCPI, T_{PRI} is the PRI time period and α_j is the weights that the radar assigns to the pulses. The weights are generally set to $1/J$ to simply average the pulses. With Equation 14 incorporated into the overall ambiguity we obtain the full integral equation,

$$\rho(\tau_s, \mathbf{r}_s, t_s) = \int L(\tau_s, \mathbf{r}_s, t_s, \tau, \mathbf{r}, t) R(\tau, \mathbf{r}, t) dV dt. \quad (15)$$

The final kernel, $L(\tau_s, \mathbf{r}_s, t_s, \tau, \mathbf{r}, t) = G(t_s, t)K(\tau_s, \mathbf{r}_s, \tau, \mathbf{r})$, encompasses the full space-time ambiguity.

2.3. Ambiguity after Frame Transformation

We will now focus on the impact of the motion of plasma as it is going through the field of view of the radar. We will assume that the radar is integrating over a length of time T beginning at t_s . The kernel L will be represented as a separable function K and G as in Equation 15. In this case, G will be a summation of Dirac delta functions with weights of $1/J$. This will change Equation 15 to the following:

$$\rho(\tau_s, \mathbf{r}_s, t_s) = \int K(\tau_s, \mathbf{r}_s, \tau, \mathbf{r}) \left[(1/J) \int_{t_s}^{t_s+T} \sum_{j=0}^{J-1} \delta(t - t_s - jT_{PRI}) R(\tau, \mathbf{r}, t) dt \right] dV. \quad (16)$$

Of specific interest in this study are instances in the high latitude ionosphere where embedded plasma structures are moving due to electric field drivers applied by the magnetosphere. In this case, it will be assumed that the plasma is a rigid object and will not deform with respect to \mathbf{r} over time period $[t_0, t_0 + T]$ where $T = JT_{PRI}$ is the time for one NCPI. Also, it will be assumed that the plasma parcel moves with a constant velocity \mathbf{v} . Thus $R(\tau, \mathbf{r}, t) \Rightarrow R(\tau, \mathbf{r} + \mathbf{v}t)$. The assumption of rigidity is valid over the time period of the NCPI, on the order of a few minutes, while the plasma moves through the field of view of the radar. For example, in the high latitude ionosphere, large scale features in structures such as patches decay on the order of hours [Tsunoda, 1988]. This assumption is useful because it allows our framework to analyze impacts of these plasma variations on the parameter resolution of ISR systems. With these assumptions, Equation 16 becomes,

$$\rho(\tau_s, \mathbf{r}_s, t_s) = (1/J) \int \int_{t_s}^{t_s+T} \sum_{j=0}^{J-1} \delta(t - t_s - jT_{PRI}) K(\tau_s, \mathbf{r}_s, \tau, \mathbf{r}) R(\tau, \mathbf{r} + \mathbf{v}t) dt dV \quad (17)$$

A change of variables to $\mathbf{r}' = \mathbf{r} + \mathbf{v}t$ acts as a Galilean transform and applies a warping to the kernel, changing the frame of reference. Since $R(\tau, \mathbf{r}')$ is no longer dependent on t , Equation 17 can be integrated in time and becomes:

$$\rho(\tau_s, \mathbf{r}_s, t_s) = (1/J) \int \left[\sum_{j=0}^{J-1} K(\tau_s, \mathbf{r}_s, \tau, \mathbf{r}' - \mathbf{v}(t_s + jT_{PRI})) \right] R(\tau, \mathbf{r}') dV. \quad (18)$$

The problem can now be simplified further back to a Fredholm integral equation by simply replacing the terms in the square brackets as a new kernel $A(\tau_s, \mathbf{r}_s, t_s, \tau, \mathbf{r}')$:

$$\rho(\tau_s, \mathbf{r}_s, t_s) = \int A(\tau_s, \mathbf{r}_s, t_s, \tau, \mathbf{r}') R(\tau, \mathbf{r}') dV. \quad (19)$$

The impact of the plasma velocity on the ambiguity function can be seen in Figure 4. This is the same ambiguity as seen in Figure 3 but with a velocity of 500 m/s in the y direction over a period of 2 minutes. This velocity creates a larger ambiguity function in the frame of reference of the moving plasma.

The operator A can be determined through knowledge of the radar system's beam pattern along with the experiment's pulse pattern, integration time and inherent velocity of the plasma. This velocity \mathbf{v} can be separately estimated by taking measurements of the Doppler shift and using a methodology seen in *Butler et al.* [2010]. Once the operator has been determined, standard processing techniques can be used as if the plasma is not moving, under the previous assumptions.

3. Simulation

Although Figures 3 and 4 show the spatial extent of the space-time ambiguity function both with and without target motion, the impact of this on the reconstruction data can better be shown through simulation. To do so, we present in this section data from a 3-D ISR simulator with a known set of ionospheric parameters. In the following section, we describe this simulator along with two case studies to show the impact of this ambiguity on properly reconstructing ionospheric plasma parameters.

3.1. Simulator

The 3-D ISR simulator creates data by deriving a time filter from the autocorrelation functions and applying them to complex white Gaussian noise generators. Stating this in another way, every point in time and space has a noise plant and filter structure as in Figure 5. The data is then scaled and summed together according to its location in range and angle space to radar. For this simulation, data points are only used if they are within 1.1° of the center beam which is a simplification of the AMISR beam pattern.

After the IQ data has been created it is processed to create estimates of the ACF at desired points of space. This processing follows a flow chart seen in Figure 6.

The sampled I/Q voltages can be represented as $x(n_s) \in \mathbb{C}^N$ where N is the number of samples in an inter pulse period. At this point, the first step in estimating the autocorrelation function is taken. For each range gate $m \in 0, 1, \dots, M-1$ an autocorrelation is estimated for each lag of $l \in 0, 1, \dots, L-1$. This operation of forming the ACF estimates repeats for each pulse, $j \in 0, 1, \dots, J-1$, and is then summed over the J pulses. The entire operation to form the initial estimate of $\hat{R}(m, l)$ is the following,

$$\hat{R}(m, l) = \sum_{j=0}^{J-1} x(m - \lfloor l/2 \rfloor, j) x^*(m + \lceil l/2 \rceil, j). \quad (20)$$

The case shown in Equation 20 is a centered lag product, which is what has been used for our simulations, but other types of lag product calculations are possible as well. In the centered lag product case, range gate index m and sample index n

can be related by $m = n_s - \lfloor L/2 \rfloor$ and the maximum lag and sample relation is
 $M = N - \lceil L/2 \rceil$.

After the lag products have been formed, an estimate of the noise correlation is
 subtracted out of $\hat{R}(m, l)$, defined as $\hat{R}_w(m, l)$,

$$\hat{R}_w(m_w, l) = \sum_{j=0}^{J-1} w(m_w - \lfloor l/2 \rfloor, j) w^*(m_w + \lceil l/2 \rceil, j), \quad (21)$$

where $w(n_w)$ is the background noise process of the radar.

The final estimate of the autocorrelation function after the noise subtraction and
 summation rule will be represented by $\hat{R}_f(m, l)$. At this point, a summation rule is
 applied and the data is sent off to be fit. The final parameters are derived through
 a standard Levenberg-Marquardt non-linear least-squares fitting [*Levenberg*, 1944]
 producing plasma parameter scalar values of electron density, electron temperature,
 ion temperature, and ion composition.

3.2. Case 1: Electron Density Perturbation

A first example of the simulation described in the previous sections is a simple case
 of a small plasma enhancement moving through the radar field of view. This case
 is meant to model conditions expected in the polar cap ionosphere under southward
 IMF conditions [*Dahlgren et al.*, 2012b]. The background electron density is set to
 vary in altitude as a Chapman function, shown in Figure 7, while the electron and
 ion temperature remains constant.

Embedded in the background density, we place a 35 km radius sphere of enhanced
 electron density of $5 \times 10^{10} \text{ m}^{-3}$ centered at 400 km altitude and moving at 500 m/s

velocity along the y direction. Images from this phantom can be seen in Figure 8. To simplify the simulation, the ionospheric composition is assumed to be 100% oxygen ions. For ease of comparison, the phantom is only shown in areas where it is in the radar's field of view. The positions of the 11 x 11 beam grid used for this case can be seen in Figure 9.

Because only the electron density is varying, the fitting method in this case becomes simply a power estimate, as incoherent scatter theory predicts that the electron density is directly proportional to the scattered power if the ion-to-electron temperature ratio is known. This example allows easier observation of the blurring from the space-time ambiguity function, while also demonstrating trade offs between statistical variance and blurring.

Using the phantom, we can see how changing only the integration time can impact the reconstruction. In Figure 10 we plot a case where only 10 pulses are used in each direction for the reconstruction, corresponding to an integration time of about 9 seconds. The enhancement can be seen as it moves through the field of view, although there is a high amount of variance in the reconstruction. Figure 11 shows the reconstruction with 200 pulses in each direction, or 3 minute total integration time. The variability has been reduced but there is a large amount of blurring of the enhancement as it moves through the field of view.

In order to give a comparison based on integration time, a phantom was also created with no motion. This can be seen in the first pane of Figure 12. An image using the same integration time as in Figure 10 for the stationary phantom is shown as the

center pane in Figure 12. Another image using the longer integration time can be seen in the right pane of Figure 12. These images show that the blurring is on the same order between both integration times.

3.3. Case 2: Plasma Temperature and Density Perturbation

We present a second case of a simulation of the plasma density enhancement through the field of view, during which the ion and electron temperatures are allowed to vary. This case is a departure from the standard blurring problem seen in image processing, because the plasma parameters to be estimated are related to the observable ACF through a non-linear expression. However, the resulting ACF estimates are created through a linear blurring kernel in both time and space.

We again use a plasma enhancement moving through the field of view at 500 m/s, but the electron and ion temperature varies with time and altitude. The background ion and electron temperature vs. height can be seen in Figure 14. As the electron density enhancement feature travels through the field of view, the ion and electron temperature ratio is set to drop by the same ratio that the electron density is enhanced. This is done to keep the variance the same at each point in space for a given number of pulses integrated.

The phantoms for each parameter at approximately 402 seconds can be seen in Figure 14. The reconstruction of this field at the same time can be seen in Figure 15. Note that the reconstruction does not seem to show the electron density enhancement, even in a blurred form.

In order to determine the reason behind the poor reconstruction, we look at the fit surface of one of the points in the reconstruction. The fit surface is the error between the estimated ISR spectrum and the spectrum derived from the different parameters. We will compare the points $\mathbf{r} = [10, 10, 400]$ km and the closest reconstruction point in the radar field of view, $\mathbf{r}_s = [6.72, 1.80, 398.77]$ at time 309.5s. The time was chosen so the integrated measurement would be centered over the interval when the enhancement moved through this point, as the radar will integrate over two distinct plasma distributions. The plasma parameters at point \mathbf{r} are $N_e = 1.96 \times 10^{10} \text{m}^{-3}$, $T_i = 1064$ K and $T_e = 1324$ K when there is no enhancement traveling through. When the enhancement is traveling through this point $N_e = 5 \times 10^{10} \text{m}^{-3}$, $T_i = 416$ K and $T_e = 518$ K. The speed of the enhancement, 500 m/s, causes about two-thirds of the pulses measured to correspond to the enhanced plasma during the integration.

After integrating and fitting the ISR spectra, the parameter fit results at \mathbf{r} are $N_e = 2.36 \times 10^{10} \text{m}^{-3}$, $T_i = 973$ K and $T_e = 500$ K, representative of neither the background or enhanced plasma. To investigate further, the fit surface was formed over the parameter space of $N_e = 1 \times 10^{10}$ to $1 \times 10^{11} \text{m}^{-3}$, and for both T_e and T_i over values 100 to 1500 °K. In this case, the fit surface showed that the global minimum was located in the same location as found by the Levenberg-Marquardt algorithm. A two dimensional cut of the fit surface variation as a function of T_i and T_e holding $N_e = 2.43 \times 10^{10} \text{m}^{-3}$ is shown in Figure 16. The final fit values are located at a global minimum, indicating that this is not a result of multiple parameter ambiguities but rather that the non uniformity of the plasma parameters caused an

erroneous fit. Mixtures of different plasma populations causing erroneous fits have been shown before such as in *Knudsen et al.* [1993].

For further insight, power spectra calculated from the original known plasma parameters compared with those calculated from the final fit estimates can be seen in Figure 17. In this case, the spectrum estimated from the data has been reduced by averaging over time and space which has lowered its power dramatically, thus creating an ambiguous shape which also matches a spectrum with improper parameter values.

4. Possible Mitigation Techniques

As can be seen from the previous sections, a number of different types of errors can occur if the ISR measurement technique does not properly account for the full space-time ambiguity function under ionospheric variability conditions. There are a number of possible approaches one could take in order to mitigate these effects and produce an improved data product from electronically scanned ISR measurements. The discussion in this section is by no means exhaustive, but rather gives an idea of the utility of this frame work. In order to focus the discussion, we will concentrate on methods to remove motion blur type errors that occur when plasma is moving through the field of view, along with techniques to improve the spatio-temporal resolution of the measurements.

In order to reduce the impact from plasma parcel motion, a relatively simple approach would involve processing the data in the frame of reference of the moving

density field. The convection velocity is manifested as a bulk Doppler shift in the ISR spectrum. Under the uniform composition assumptions applied in our examples, this Doppler shift is independent of the other parameters, and so \mathbf{v} in Equation 18 could be extracted using the separate analysis described by *Heinselman and Nicolls* [2008] and *Butler et al.* [2010]. After measuring the velocity, instead of integrating data across slow-time in the same beam, one could integrate properly across different beams using this knowledge. This would allow a statistically stationary ACF to be formed from plasma populations with the same physical state as they move through the field of view.

To improve the plasma parameter resolution, it may also be necessary to perform some sort of regularization. There are two types of regularization that can be applied in this case. The first type is parameter based regularization, such as is employed in full profile analysis [*Holt et al.*, 1992; *Hysell et al.*, 2008]. We will use the term parameter based regularization in this case since the procedure applies constraints to the physical parameters that are determined after fitting. Full profile analysis has only been applied to date along the range dimension and not in all three spatial dimensions. However, if full profile analysis is extended so it can be used in ESA systems, a forward model between the actual ACF and the one measured in the radar would be needed. This model formulation is encompassed within Equation 15.

The second regularization method is referred to here as data based regularization. This term infers the application of constraints first to the estimates of the autocorrelation functions, after which fitting takes place. The constraints usually deal with

how the data itself changes over time and space by constraining the energy of the ACF [Virtanen *et al.*, 2008; Nikoukar *et al.*, 2008] or its derivative [Nikoukar, 2010]. A simplified description of the data based regularization lies in an equivalence with a deconvolution operation on the ACFs. This has an advantage that one can use linear inverse theory to estimate ACF lags before fitting, as opposed to parameter based regularization schemes such as full profile analysis where ionospheric parameters are directly estimated and regularized. Because of these features, data based regularization has the advantage of generally being more computationally tractable than parameter based. However, a significant drawback to data based regularization is that is very difficult to argue what constraint would be "correct" to use, while in full profile analysis the constraints are often based on likely physical variations in the ionosphere. In any case, in order to extend the methodology from Virtanen *et al.* [2008] and Nikoukar *et al.* [2008], one can use the kernel L for the case of improving measurements from an ESA ISR.

5. Conclusion

This publication has laid the foundation for the optimal analysis of volumetric data acquired from electronically steerable ISR systems. The framework developed here takes into account the full antenna beam pattern, pulse pattern and time integration. Through simulations, we have shown how plasma motion can impact reconstruction of parameters which, compounded with the non-linear nature of the parameter fitting step, can create errors which are potentially unexpected and hard to predict.

Lastly, we briefly outlined a number of possible mitigation approaches improving measurements derived from ESA ISRs.

Appendix A: Derivation of Idealized AMISR Array Pattern

The current antenna on the AMISR systems is made up 8x16 set of panel of half wave cross dipoles. Each panel has 32 cross dipoles in a 8x4 hexagonal configuration. In the current set up at the Poker Flat site this yields at 4096 element array in a 64x64 element hexagonal configuration.

In order to simplify the antenna can be treated as two rectangular arrays of cross dipoles interleaved together. In the x direction each of these arrays will have a spacing of $2d_x$ with $M/2$ elements. The y direction will be of length N elements and spacing d_y . Using basic planar phase array theory, [Balanis, 2005], we can start with the linear array pattern from the first array can be represented as

$$E_1(\theta, \phi) = \sum_{m=1}^{M/2} \sum_{n=1}^N \exp[-j2(m-1)kd_x \sin \theta \cos \phi - j(n-1)kd_y \sin \theta \sin \phi]. \quad (\text{A1})$$

Since the second array can be thought of a shifted version of the first in the x direction we get the following

$$E_2(\theta, \phi) = \sum_{m=1}^{M/2} \sum_{n=1}^N \exp[-j(2m-1)kd_x \sin \theta \cos \phi - j(n-1/2)kd_y \sin \theta \sin \phi]. \quad (\text{A2})$$

In order to simplify notation we will make the following substitutions, $\psi_x = -kd_x \sin \theta \cos \phi$, $\psi_y = -kd_y \sin \theta \sin \phi$. Using Equations A1 and A2 we can see the following relationship,

$$E_2(\theta, \phi) = \exp [j(\psi_y/2 + \psi_x)] E_1(\theta, \phi) = \sum_{m=1}^{M/2} \sum_{n=1}^N \exp [-j2(m-1)\psi_x - j(n-1)\psi_y]. \quad (\text{A3})$$

Adding E_1 and E_2 together we get the following linear array pattern

$$\begin{aligned} E(\theta, \phi) &= (1 + \exp [j(\psi_y/2 + \psi_x)]) \sum_{m=1}^{M/2} \sum_{n=1}^N \exp [-j2(m-1)\psi_x - j(n-1)\psi_y]. \\ &= \frac{1}{MN} (1 + \exp [j(\psi_y/2 + \psi_x)]) \frac{\sin((M/2)\psi_x)}{\sin(\psi_x/2)} \frac{\sin((N/2)\psi_y)}{\sin(\psi_y/2)}. \end{aligned} \quad (\text{A4})$$

Since the array is steerable this can be taken into account in the equations by simply changing the definitions of ψ_x and ψ_y to $\psi_x = kd_x(\sin \theta \cos \phi - \sin \theta_s \cos \phi_s)$, and $\psi_y = kd_y(\sin \theta \sin \phi - \sin \theta_s \sin \phi_s)$. Lastly the antenna pattern of a single cross dipole can be represented as $\frac{1}{2}(1 + \cos^2(\theta))$ [Balanis, 2005]. By taking the squared magnitude of the array factor and multiplying it with the pattern of the dipole we get Equation 11,

$$F(\theta_s, \phi_s, \theta, \phi) = \frac{1}{2}(1 + \cos^2(\theta)) \left| \frac{1}{MN} (1 + \exp [j(\psi_y/2 + \psi_x)]) \frac{\sin((M/2)\psi_x)}{\sin(\psi_x/2)} \frac{\sin((N/2)\psi_y)}{\sin(\psi_y/2)} \right|^2. \quad (\text{A5})$$

References

- 410 Balanis, C. A. (2005), *Antenna Theory: Analysis and Design*, Wiley-Interscience.
- 411 Butler, T. W., J. Semeter, C. J. Heinselman, and M. J. Nicolls (2010), Imaging f
412 region drifts using monostatic phased-array incoherent scatter radar, *Radio Sci.*,
413 45(5), RS5013, doi:10.1029/2010RS004364.
- 414 Dahlgren, H., J. L. Semeter, K. Hosokawa, M. J. Nicolls, T. W. Butler, M. G. Johnsen,
415 K. Shiokawa, and C. Heinselman (2012a), Direct three-dimensional imaging of polar
416 ionospheric structures with the resolute bay incoherent scatter radar, *Geophysical*
417 *Research Letters*, 39(5), doi:10.1029/2012GL050895.
- 418 Dahlgren, H., G. W. Perry, J. L. Semeter, J. P. St. Maurice, K. Hosokawa, M. J.
419 Nicolls, M. Greffen, K. Shiokawa, and C. Heinselman (2012b), Space-time variabil-
420 ity of polar cap patches: Direct evidence for internal plasma structuring, *Journal*
421 *of Geophysical Research: Space Physics*, 117(A9), doi:10.1029/2012JA017961.
- 422 Dougherty, J. P., and D. T. Farley (1960), A theory of incoherent scattering of
423 radio waves by a plasma, *Proceedings of the Royal Society of London. Series A,*
424 *Mathematical and Physical Sciences*, 259(1296), pp. 79–99.
- 425 Dougherty, J. P., and D. T. Farley (1963), A theory of incoherent scattering of radio
426 waves by a plasma, 3 scattering in a partly ionized gas, *Journal of Geophysical*
427 *Research*, 68, 5473.
- 428 Farley, D. T. (1969), Incoherent scatter correlation function measurements, *Radio*
429 *Sci.*, 4(10), 935–953.

- 430 Farley, D. T., J. P. Dougherty, and D. W. Barron (1961), A theory of incoherent
431 scattering of radio waves by a plasma ii. scattering in a magnetic field, *Proceedings*
432 *of the Royal Society of London. Series A, Mathematical and Physical Sciences*,
433 *263*(1313), pp. 238–258.
- 434 Hagfors, T. (1961), Density fluctuations in a plasma in a magnetic field, with ap-
435 plications to the ionosphere, *Journal of Geophysical Research*, *66*(6), 1699–1712,
436 doi:10.1029/JZ066i006p01699.
- 437 Heinselman, C. J., and M. J. Nicolls (2008), A bayesian approach to electric field and
438 e-region neutral wind estimation with the poker flat advanced modular incoherent
439 scatter radar, *Radio Science*, *43*(5), doi:10.1029/2007RS003805.
- 440 Holt, J. M., D. A. Rhoda, D. Tetenbaum, and A. P. van Eyken (1992), Optimal
441 analysis of incoherent scatter radar data, *Radio Science*, *27*(3), 435–447, doi:
442 10.1029/91RS02922.
- 443 Hysell, D. L., F. S. Rodrigues, J. L. Chau, and J. D. Huba (2008), Full profile
444 incoherent scatter analysis at jicamarca, *Annales Geophysicae*, *26*(1), 59–75, doi:
445 10.5194/angeo-26-59-2008.
- 446 Knudsen, D. J., G. Haerendel, S. Buchert, M. C. Kelley, Å. Steen, and U. Brändström
447 (1993), Incoherent scatter radar spectrum distortions from intense auroral turbu-
448 lence, *Journal of Geophysical Research: Space Physics*, *98*(A6), 9459–9471, doi:
449 10.1029/93JA00179.
- 450 Lehtinen, M. S., and A. Huuskonen (1996), General incoherent scatter analysis and
451 {GUISDAP}, *Journal of Atmospheric and Terrestrial Physics*, *58*(1–4), 435 – 452,

doi:[http://dx.doi.org/10.1016/0021-9169\(95\)00047-X](http://dx.doi.org/10.1016/0021-9169(95)00047-X).

Levenberg, K. (1944), A method for the solution of certain non-linear problems in least squares, *Quarterly of Applied Mathematics*, *2*, 164–168.

Nicolls, M. J., and C. J. Heinselman (2007), Three-dimensional measurements of traveling ionospheric disturbances with the Poker Flat Incoherent Scatter Radar, *Geophysical Research Letters*.

Nikoukar, R. (2010), Near-optimal inversion of incoherent scatter radar measurements- coding schemes, processing techniques, and experiments, Ph.D. thesis, University of Illinois at Urbana-Champaign.

Nikoukar, R., F. Kamalabadi, E. Kudeki, and M. Sulzer (2008), An efficient near-optimal approach to incoherent scatter radar parameter estimation, *Radio Science*, *43*(5), doi:10.1029/2007RS003724.

Richards, M. A. (2005), *Fundamentals of Radar Signal Processing*, McGraw-Hill.

Semeter, J., T. Butler, C. Heinselman, M. Nicolls, J. Kelly, and D. Hampton (2009), Volumetric imaging of the auroral ionosphere: Initial results from pfisr, *Journal of Atmospheric and Solar-Terrestrial Physics*, *71*, 738 – 743, doi:10.1016/j.jastp.2008.08.014.

Tsunoda, R. T. (1988), High-latitude F region irregularities: A review and synthesis, *Reviews of Geophysics*.

Virtanen, I. I., M. S. Lehtinen, T. Nygrén, M. Orispää, and J. Vierinen (2008), Lag profile inversion method for eiscat data analysis, *Annales Geophysicae*, *26*(3), 571–581, doi:10.5194/angeo-26-571-2008.

474 Zettergren, M., J. Semeter, P.-L. Blelly, G. Sivjee, I. Azeem, S. Mende, H. Gleisner,
475 M. Diaz, and O. Witasse (2008), Optical estimation of auroral ion upflow: 2. a
476 case study, *Journal of Geophysical Research: Space Physics*, 113(A7), n/a–n/a,
477 doi:10.1029/2008JA013135.

478 **Acknowledgments.** This work was supported by the National Science Founda-
479 tion, through Aeronomy Program Grant AGS-1339500 to Boston University and
480 Cooperative Agreement AGS-1242204 between the NSF and the Massachusetts In-
481 stitute of Technology, and by the Air Force Office of Scientific Research under contract
482 FA9550-12-1-018. The authors are grateful to the International Space Science Insti-
483 tute (ISSI, Bern, Switzerland) for sponsoring a series of workshops from which the
484 idea for this work emerged.

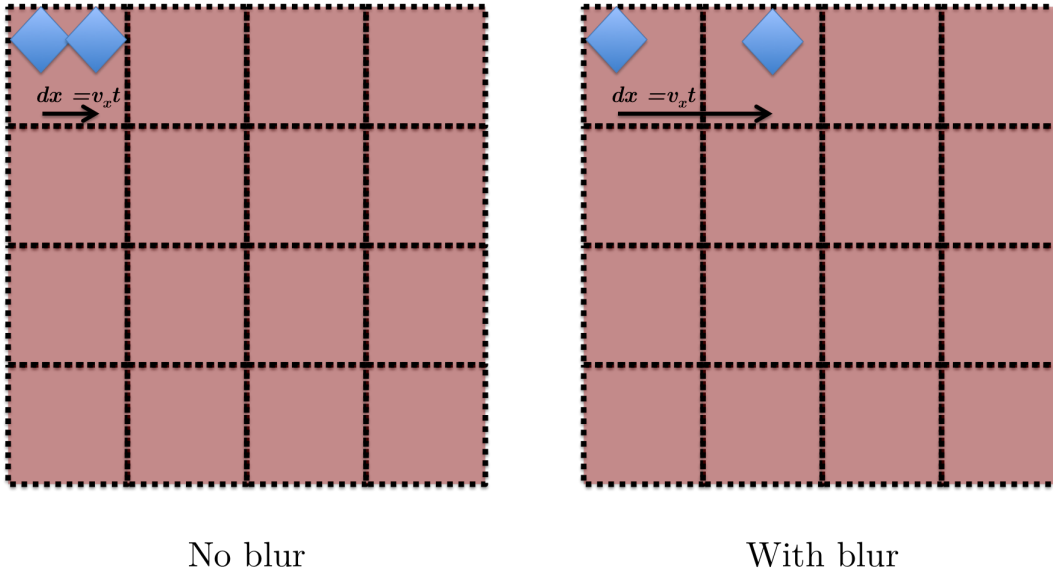


Figure 1. CCD resolution cell diagram both with and without blurring

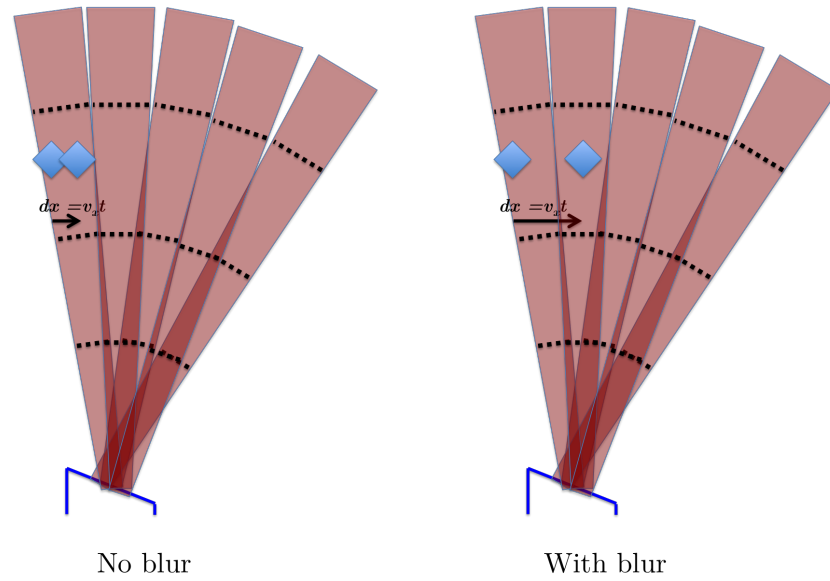


Figure 2. ISR resolution cell diagram both with and without blurring

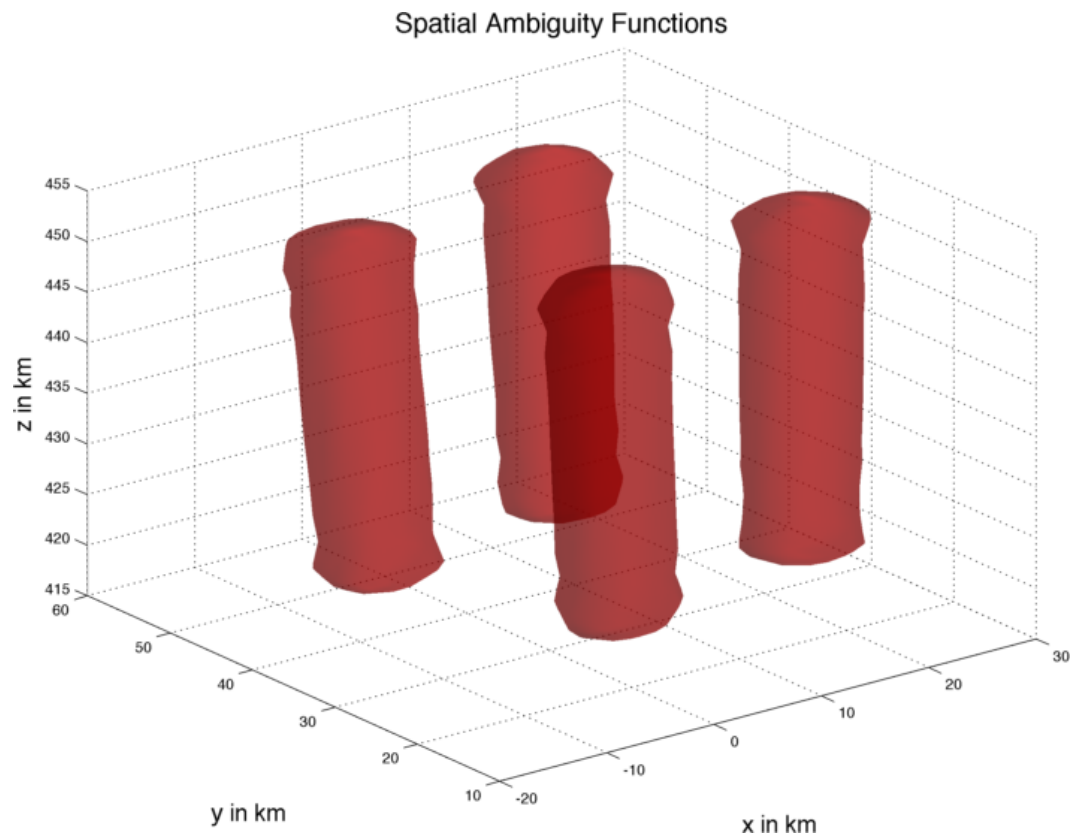


Figure 3. Full spatial ambiguity function

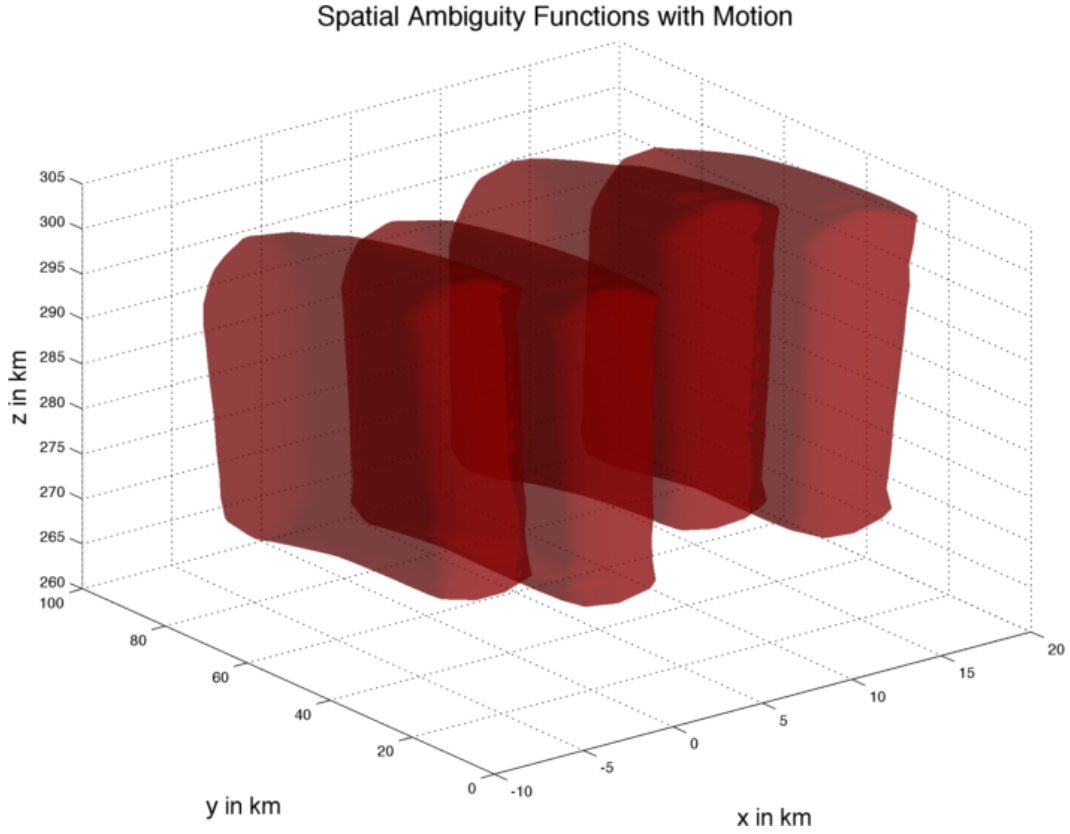


Figure 4. Full spatial ambiguity function with target motion

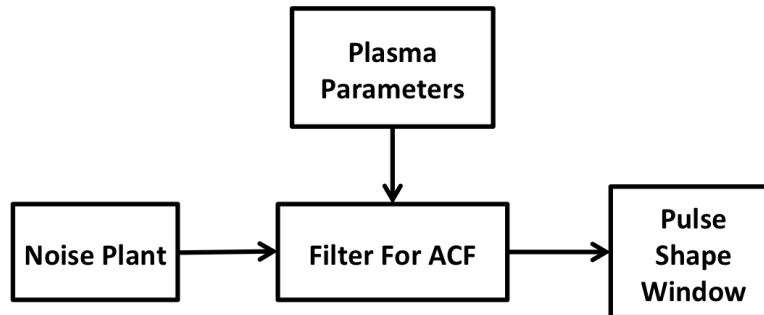


Figure 5. I/Q simulator signal flow diagram.

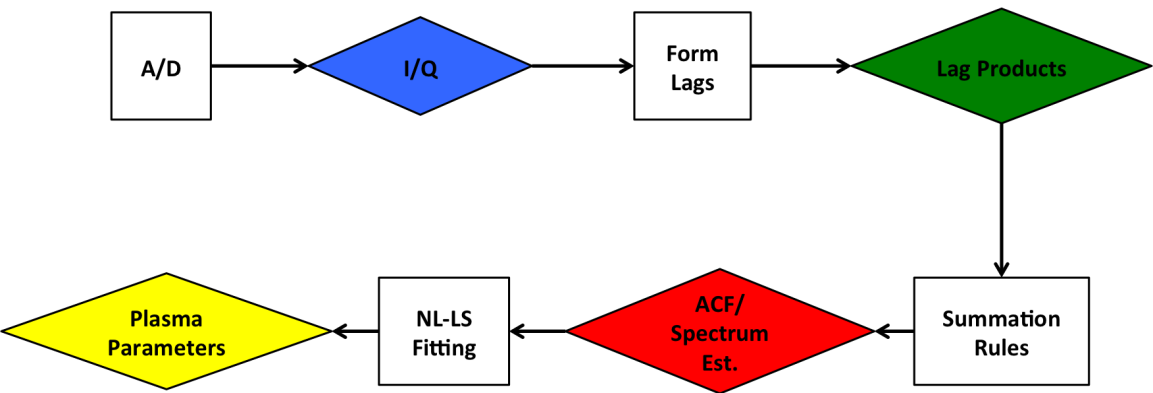


Figure 6. ISR processing chain.

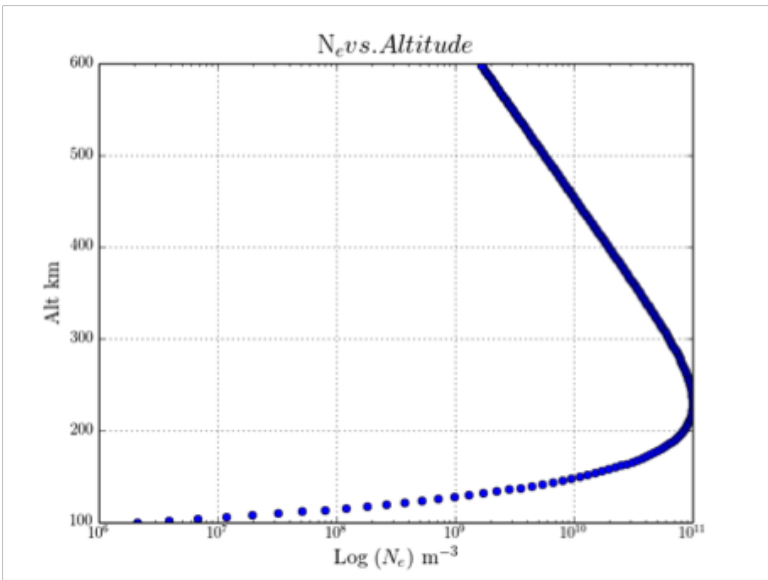


Figure 7. Simulated electron density verses altitude.

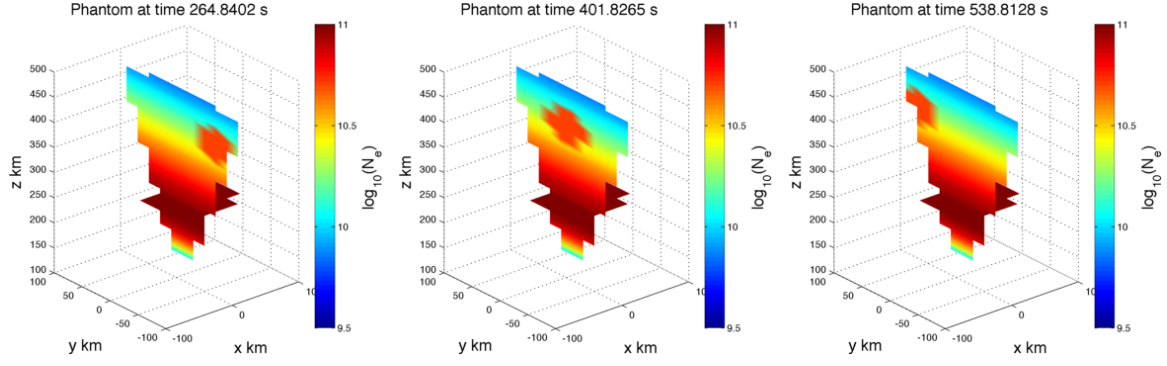


Figure 8. Images of input N_e for the simulation at three different times.

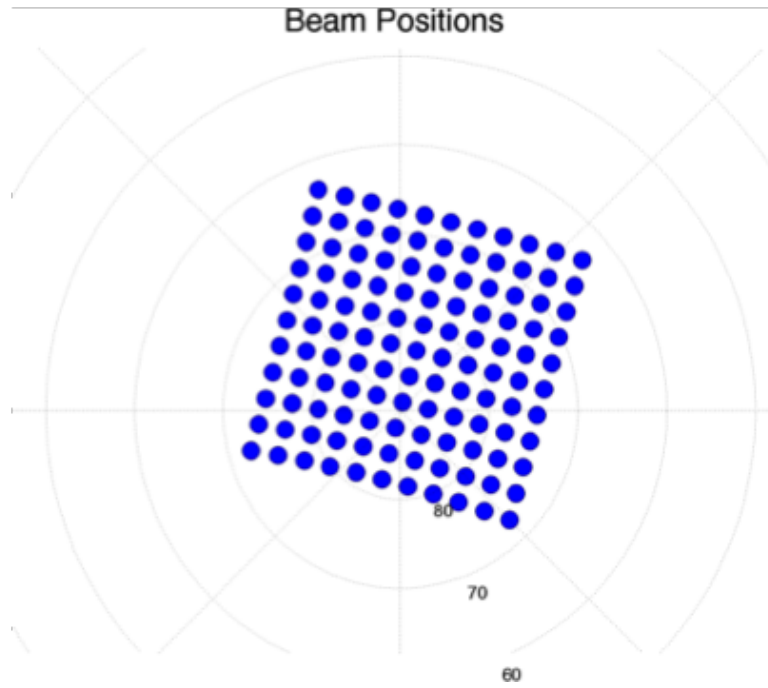


Figure 9. Radar beam pattern used in the simulations

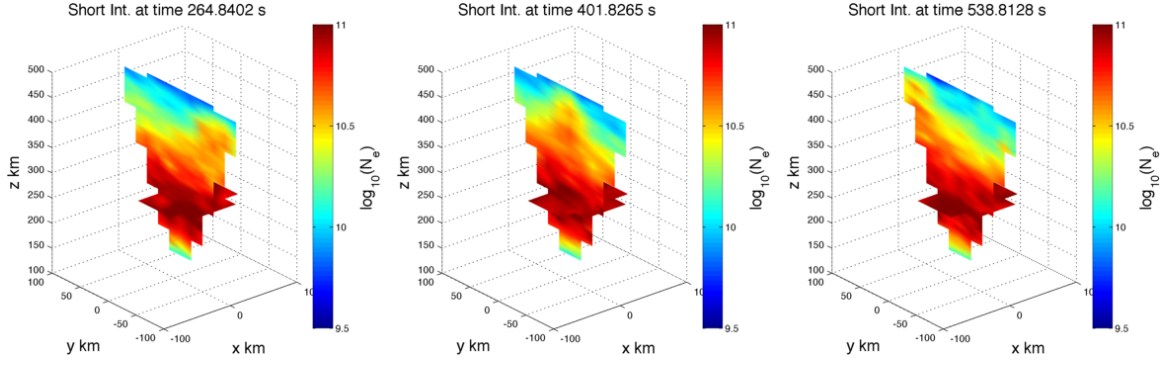


Figure 10. Reconstructions of N_e using 10 Pulses at three different times.

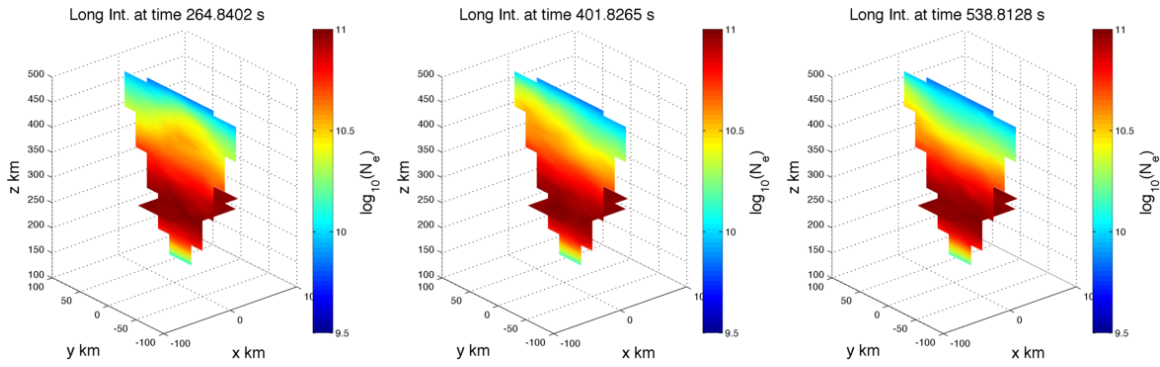


Figure 11. Reconstructions of N_e using 200 Pulses at three different times.

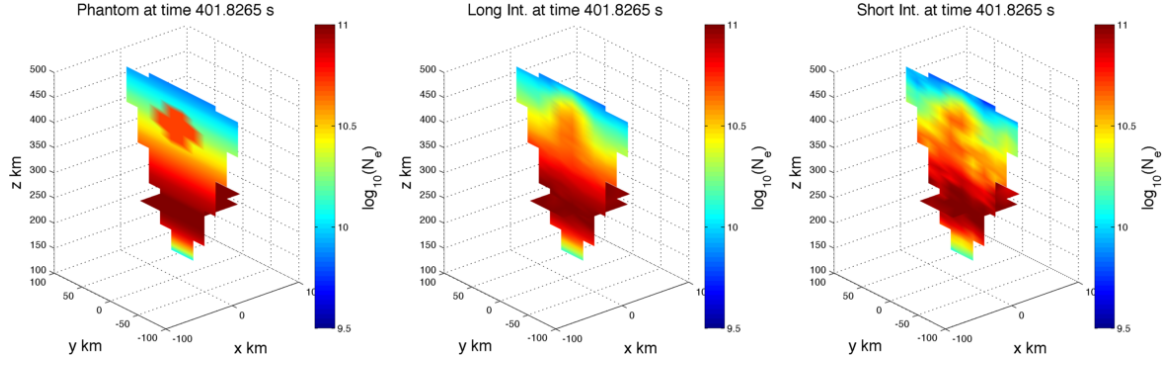


Figure 12. Stationary phantom of N_e along with reconstructions using 10 and 200 pulses.

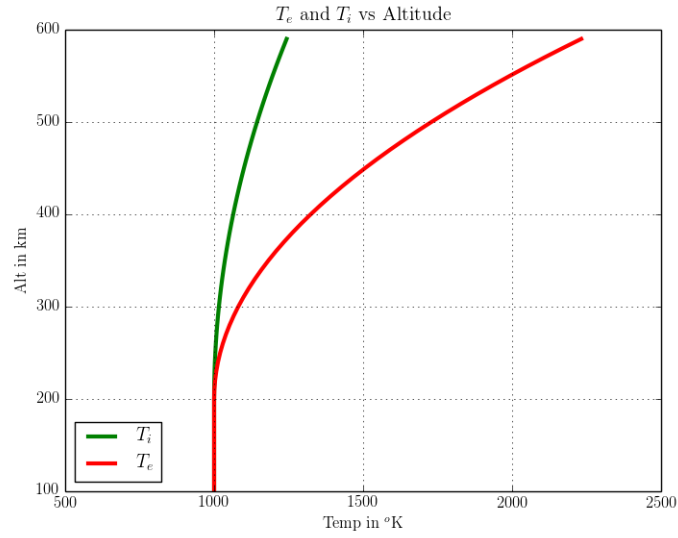


Figure 13. Ion & electron temperature verses height for simulation.

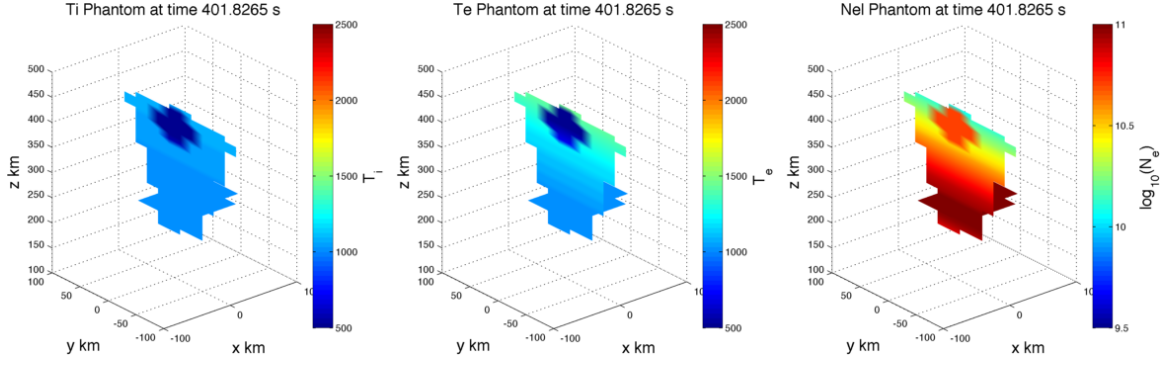


Figure 14. Phantoms of T_i , T_e and N_e at $t = 401.8265$ s.

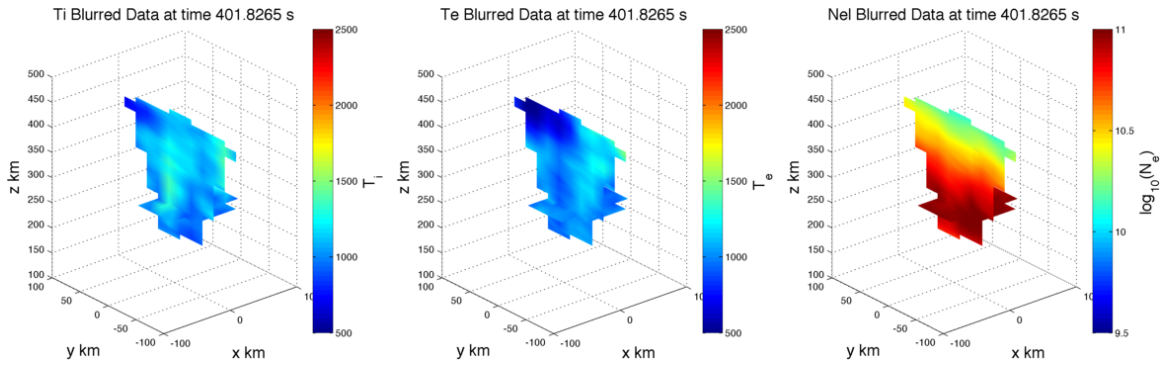


Figure 15. Interpolated reconstructions of T_i , T_e and N_e at $t = 401.8265$ s.

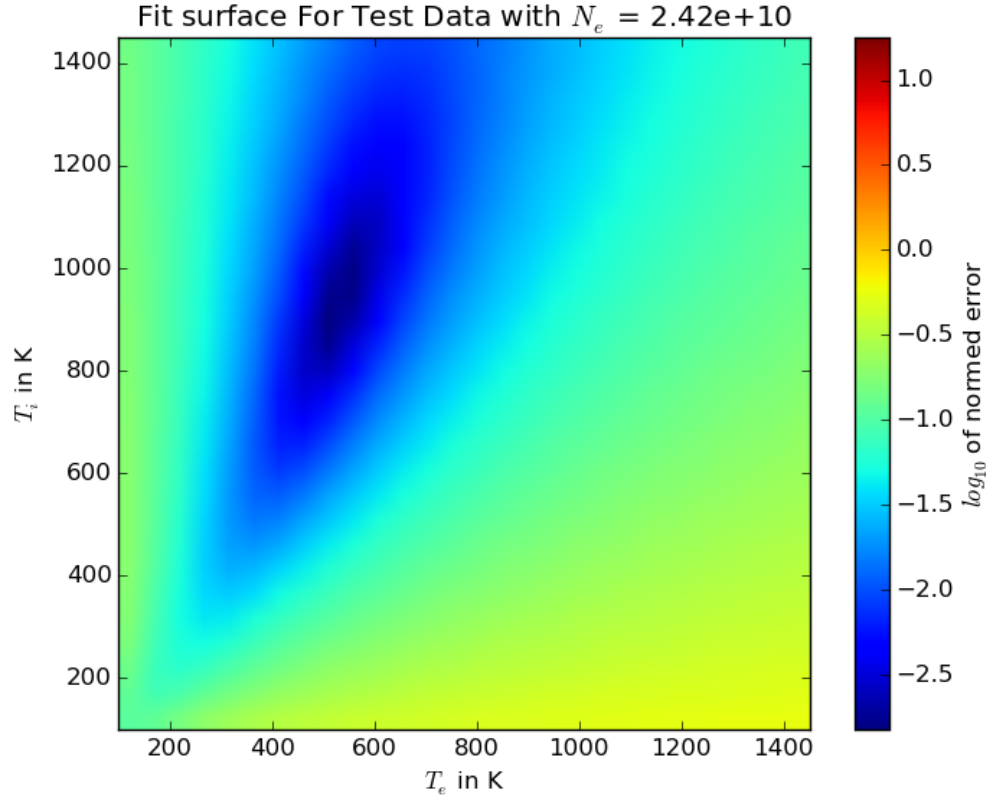


Figure 16. Fit surface spectrum at $\mathbf{r}_s = [6.72, 1.80, 398.77]$.

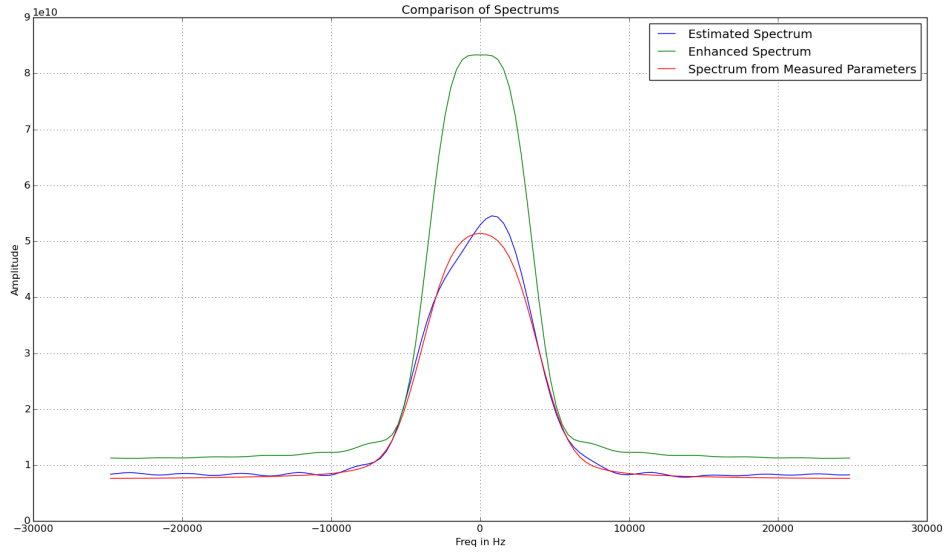


Figure 17. Estimated spectrum from $\mathbf{r}_s = [6.72, 1.80, 398.77]$ along with spectrum from measured parameters and from enhanced plasma.